Direct numerical simulations of compressible three-layer Rayleigh–Taylor instability

Orkun Mert Ustun *
The University of Alabama, Tuscaloosa, AL, 35487, USA

Denis Aslangil†
The University of Alabama, Tuscaloosa, AL 35487, USA

Man Long Wong
Stanford University, Stanford, CA 94305, USA

Multi-fluid mixing in a system with three stratified layers is explored using two-dimensional compressible direct numerical simulations (DNS) by solving fully compressible multi-species Navier–Stokes equations. All configuration cases under investigation consist of at least one acceleration-driven Rayleigh–Taylor unstable interface where the direction of the acceleration is from the heavier to the lighter fluids to initiate the chaotic mixing. The DNS are initialized with isopycnic background stratification, where the species densities of the three fluids are initially constant over the domain, and also they are benefited from the adaptive mesh refinement (AMR) to reduce the computational cost. We investigate four cases with the global Atwood number of 0.04 where the stratified layers along the acceleration direction (from bottom to top) have heavy-intermediate-light, heavy-light-light, heavy-light-intermediate, and heavy-light-heavy densities, and each case is studied with two different distances between the first and third fluid layers. It is found that the globally unstable case with heavy-intermediate-light densities, which has two unstable interfaces, exhibits symmetric mixing during the flow evolution and eventually behaves similarly to the classical two-layer Rayleigh–Taylor instability (RTI) flows. This finding is consistent with the observation in previous three-layer RTI experiments. The case with heavy-light-light densities is performed for comparison purposes, and it practically only has a single-stratified interface similar to the two-layer RTI problem. For the remaining two cases, the top interface of the three-layer RTI is stably stratified. It is shown that for the cases where the top interface is neutrally stratified (e.g., heavy-light-light case) or weakly stratified (e.g., heavy-light-intermediate case), upward pure fluids penetration is larger compared to the heavy-light-heavy case, whose top interface is initially strongly stable. In addition to the study on large-scale RTI entrainment, we also present mixedness and vortical dynamics of the flows.

I. Introduction

Rayleigh–Taylor instability (RTI) refers to a hydrodynamic instability in a fluid system in which there is an acceleration in the opposite direction of the density gradient [1, 2]. RTI is observed in a variety of flows and applications, including convection-driven atmospheric, oceanic, and geologic flows, astrophysical flows, inertial confinement fusion (ICF), and in the mixing stage of the ramjets and scramjets [3–6]. Although RTI is often observed in applications where there are more than two involving fluids, RTI is mostly studied only with a simple two-fluid two-layer stratified configuration where the heavier fluid interacts with the lighter fluid in the presence of a constant acceleration field [7, 8]. An extension to the study of the classical RTI is the investigation under variable acceleration histories that include acceleration-deceleration-acceleration stages [9–11]. It is shown that during the deceleration stage, the RTI mixing layer width becomes well mixed, and it separates the pure light and heavy fluids and acts like "an additional fluid layer". Such a layer changes the flow dynamics during the re-acceleration stage, and it is shown that the RTI growth and its mixing are highly sensitive to the dynamics of the middle layer[11]. However, the effects of an actual additional layer that arises due to the presence of the third fluid are still relatively unexplored. Currently, there are only a few experimental studies that investigate three-layer RTI flow with one unstable and one stable interface [12, 13]. Findings of these studies

*Ph.D. Student, the Department of Aerospace Engineering & Mechanics, and AIAA Member.
†Assistant Professor, the Department of Aerospace Engineering & Mechanics, and AIAA Member.

suggest that the three-layer RTI flow becomes globally unstable at late times, and the globally unstable system has similar growth with two-layer RTI flow [12].

In this study, we investigate the time evolution of the three-layer RTI, where the first unstable interface interacts with another interface that is unstable, neutrally stable, weakly stable, and strongly stable, to explore the more complex physics of three-species buoyancy-driven mixing. In addition, the effects of the initial thickness of the middle layer on the RTI growth and mixing dynamics are studied. While the chosen Mach number that characterizes the background stratification strength is around 0.15 in this study, we prefer to conduct the simulations using the fully compressible multi-species Navier–Stokes solver to completely eliminate the potential modeling errors that may arise due to the flow compressibility. A recent study on the flow compressibility effects on the growth of two-layer isothermally stratified RTI has shown significant sensitivity of the compressible RTI to the background isothermal Mach number where an increase in the background compressibility can largely suppress the growth of the RTI mixing layer even when the background Mach number under study is in the range of 0.15 to 0.45 [14].

In the classical two-layer RTI, the density contrast is represented by the Atwood number, A, at the interface separating the two mixing fluids. By assuming both fluids are ideal gases, A is defined as:

$$A = \frac{M_H - M_L}{M_H + M_L} = \frac{\rho_H - \rho_L}{\rho_H + \rho_L}, \tag{1}$$

where M_H and M_L are the molecular weights of the heavy and light fluids, respectively, while ρ_H and ρ_L are the initial species densities of the heavy and light fluids.

A schematic visualization of the three-layer RTI is presented in Figure 1 where the acceleration points upward. As it is seen, initially, there are two interfaces. The first (lower) interface is between fluids 1 and 2 and is located at the lower half of the domain ($x/\lambda_0 < 0$). The second (upper) interface is between fluids 2 and 3 and is located at the upper half of the domain ($x/\lambda_0 > 0$). As a result, there are two interfacial values and one global value for the Atwood number. We define the global Atwood number for the three-layer RTI, A_0, as follows:

$$A_0 = \frac{M_H - M_L}{M_H + M_L} = \frac{\rho_H - \rho_L}{\rho_H + \rho_L}, \tag{2}$$

where M_H and M_L here are defined as the molecular weights of the **heaviest** and **lightest** fluids within the system, respectively, while ρ_H and ρ_L are the initial species densities of the heaviest and lightest fluids globally. The Atwood number at the first (lower) interface, A_1, is defined as:

$$A_1 = \frac{M_1 - M_2}{M_1 + M_2} = \frac{\rho_1 - \rho_2}{\rho_1 + \rho_2}, \tag{3}$$

where M_1 and M_2 are the molecular weights of fluids 1 and 2, respectively, while ρ_1 and ρ_2 are the initial species densities of fluids 1 and 2 as shown in Figure 1. Similarly, the Atwood number at the second (upper) interface, A_2, is defined as:

$$A_2 = \frac{M_2 - M_3}{M_2 + M_3} = \frac{\rho_2 - \rho_3}{\rho_2 + \rho_3}, \tag{4}$$

where M_2 and M_3 are the molecular weights of fluids 2 and 3, respectively, while ρ_2 and ρ_3 are the initial species densities of fluids 2 and 3 as shown in Figure 1. As noted, due to the definitions of the interfacial Atwood numbers, they can take value of zero when the interface is neutrally stratified ($\rho_2 = \rho_3$), positive value when the interface is unstably stratified ($\rho_2 > \rho_3$), or negative values when the interface is stably stratified ($\rho_2 < \rho_3$). The results of this study indicate that in the case which has two unstable interfaces, the RTI growth becomes like a classical two-layer RTI at late times. In addition, the differences in the mixing and the growth of vortical structures between the cases when the second (top) interface is neutrally stratified, unstably stratified, and stably stratified are studied in details.

In this study, Section II describes the governing equations and details of the investigated two-dimensional (2D) direct numerical simulation (DNS) cases. Section III presents the visualization of flow fields at different times and the time evolution of statistical quantities for each case, with a discussion of the results. Finally, Section IV summarizes our findings and discusses future work.

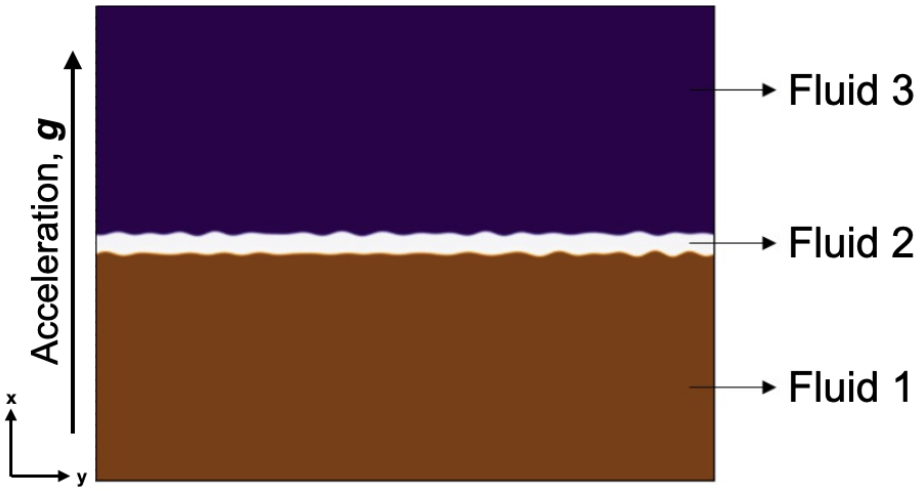

Fig. 1 Schematic visualization of three-layer RTI with three distinct fluids. The upward arrow represents the direction of the acceleration field.

II. Direct Numerical Simulations

A. Description of Governing Equations

The governing equations solved in the DNS are the compressible multi-species Navier–Stokes equations [15] with the body acceleration terms [14], which are given by

$$\frac{\partial \rho Y_i}{\partial t} + \nabla \cdot (\rho \boldsymbol{u} Y_i) = -\nabla \cdot \boldsymbol{J_i}, \quad i = 1, 2, \cdots, N, \tag{5}$$

$$\frac{\partial \rho \boldsymbol{u}}{\partial t} + \nabla \cdot (\rho \boldsymbol{u}\boldsymbol{u} + p\boldsymbol{\delta}) = \nabla \cdot \boldsymbol{\tau} + \rho \boldsymbol{g}, \tag{6}$$

$$\frac{\partial E}{\partial t} + \nabla \cdot [(E + p)\,\boldsymbol{u}] = \nabla \cdot (\boldsymbol{\tau} \cdot \boldsymbol{u} - \boldsymbol{q_c} - \boldsymbol{q_d}) + \rho \boldsymbol{g} \cdot \boldsymbol{u}, \tag{7}$$

where ρ, $\boldsymbol{u} = [u, v]^T] = [u_1, u_2]^T$, p, and E are the density, velocity vector, pressure, and total energy per unit volume, of the mixture respectively. $\boldsymbol{x} = [x, y]^T = [x_1, x_2]^T$ is the spatial coordinate vector and t is the time. Y_i is the mass fraction of the i-th species and N is the total number of species. In this work, three species are considered, i.e., $N = 3$. The constraint on mass fractions, $\sum_{i=1}^{N} Y_i = 1$, is enforced such that the mixture density is the sum of the partial densities, i.e., $\rho = \sum_{i=1}^{N} \rho Y_i$. The volume fraction of each species, Z_i, is related to the mass fraction through, $Z_i \rho_i = \rho Y_i$, where ρ_i is the species density. $\boldsymbol{g}$ is the body force acceleration vector which is assumed to be $\boldsymbol{g} = [g, 0]$ in this work. $\boldsymbol{J_i}$ is the diffusive mass flux for the i-th species. $\boldsymbol{\tau}$, $\boldsymbol{q_c}$, and $\boldsymbol{q_d}$ are the viscous stress tensor, conductive heat flux, and inter-species diffusional enthalpy flux, respectively. $\boldsymbol{\delta}$ is the Kronecker delta. All species are assumed to be at pressure and temperature equilibria. They are also assumed to be ideal and calorically perfect:

$$p = \rho_i R_i T, \tag{8}$$

$$e_i = c_{v,i} T, \tag{9}$$

where T is the mixture temperature. e_i and $c_{v,i}$ are the specific internal energy and specific heat at constant volume, respectively, of the i-th species. R_i is the specific gas constant of the i-the species provided by

$$R_i = \frac{R_g}{M_i}, \tag{10}$$

where R_g and M_i are the universal gas constant and molecular weight (or molar mass) of the i-th species. Through simple derivations, the mixture thermodynamic quantities obey the mixture ideal equation of state:

$$p = (\gamma - 1)\rho e, \tag{11}$$

$$e = c_v T = \sum_{i=1}^{N} Y_i e_i, \tag{12}$$

$$E = \rho(e + \frac{1}{2}\boldsymbol{u}\cdot\boldsymbol{u}), \tag{13}$$

where e is the specific internal energy of the mixture. γ and c_v are the ratio of specific heats and the specific heat at a constant volume of the mixture. In addition, the specific heat at a constant pressure of the mixture, c_p, is given by $c_p = \gamma c_v$.

The diffusive mass flux of each species is approximated by

$$\boldsymbol{J_i} = -\rho\left(D_i\nabla Y_i - Y_i\sum_{j=1}^{N} D_j\nabla Y_j\right), \tag{14}$$

where D_i is the effective binary diffusion coefficient or mass diffusivity of the i-th species. The Soret forces are neglected in this approximation. The effective binary diffusion coefficients are given by [16]

$$D_i = (1 - X_i)\left(\sum_{i\neq j}^{N}\frac{X_j}{\tilde{D}_{ij}}\right)^{-1}, \tag{15}$$

where $\tilde{D}_{ij}$ is the binary diffusion coefficient between species i and j, and $X_i = (M/M_i)Y_i$ is the mole fraction of the i-th species. In this work, the same binary diffusion coefficient $\tilde{D}_{ij} = D$ is assumed for all pairs of species. Through simple derivations, it can be shown that the effective binary coefficient is the same for all species, $D_i = D$, and the simple Fick's law can be recovered:

$$\boldsymbol{J_i} = -\rho D\nabla Y_i. \tag{16}$$

The mixture is assumed to be Newtonian with the viscous stress tensor $\boldsymbol{\tau}$ provided by

$$\boldsymbol{\tau} = 2\mu\boldsymbol{S} + \left(\mu_v - \frac{2}{3}\mu\right)\boldsymbol{\delta}\left(\nabla\cdot\mathbf{u}\right), \tag{17}$$

where μ and μ_v are the shear viscosity and bulk viscosity, respectively, of the mixture. The effects of bulk viscosity are neglected in this work. $\boldsymbol{S}$ is the strain-rate tensor provided by

$$\boldsymbol{S} = \frac{1}{2}\left[\nabla\boldsymbol{u} + (\nabla\boldsymbol{u})^T\right]. \tag{18}$$

The conductive heat flux and inter-species diffusional enthalpy flux [17, 18] are given by

$$\boldsymbol{q_c} = -\kappa\nabla T, \tag{19}$$

$$\boldsymbol{q_d} = \sum_{i=1}^{N} h_i\boldsymbol{J_i}, \tag{20}$$

where κ is the thermal conductivity of the mixture and h_i is the specific enthalpy of the i-th species defined by

$$h_i = c_{p,i}T, \tag{21}$$

where $c_{p,i}$ is the specific heat at constant pressure of the i-th species. The mixing rules for the fluid properties, γ, c_v, μ, and κ, are given by

$$\gamma = \frac{c_p}{c_v}, \quad c_p = \sum_{i=1}^{N} Y_i c_{p,i}, \quad c_v = \sum_{i=1}^{N} Y_i c_{v,i}, \tag{22}$$

$$\mu = \frac{\sum_{i=1}^{N}\mu_i Y_i/\sqrt{M_i}}{\sum_{i=1}^{N} Y_i/\sqrt{M_i}}, \quad \kappa = \frac{\sum_{i=1}^{N}\kappa_i Y_i/\sqrt{M_i}}{\sum_{i=1}^{N} Y_i/\sqrt{M_i}}, \tag{23}$$

where μ_i and κ_i are the dynamic viscosity and thermal conductivity, respectively. This implies that the mixture molecular weight, M, is given by

$$M = \left(\sum_{i=1}^{N} \frac{Y_i}{M_i} \right)^{-1} \tag{24}$$

In this work, the ratios of specific heats of all species are assumed to be identical with $\gamma_i = 1.4$. Thus, the fluid mixture also has a constant and uniform γ of 1.4. The kinematic viscosity, $\nu_i = \mu_i/\rho_i$, of each species are assumed to be identical for all fluids and kept constant during the simulation time, $\nu_i = \nu_0$. ν_0 is defined by the problem Reynolds number that is introduced in a later section. The fluid molecular properties are characterized by the non-dimensional Schmidt number, Sc, and the species Prandtl number, Pr_i:

$$Sc = \frac{\nu_0}{D}, \quad Pr_i = \frac{c_{p,i}\mu_i}{\kappa_i}, \tag{25}$$

Sc and Pr_i are assumed to be unity for all cases.

B. Numerical Methods

The Hydrodynamics Adaptive Mesh Refinement Simulator (HAMeRS) [15] is utilized to solve the governing equations of the DNS. HAMeRS benefits from an adaptive mesh refinement (AMR) method with local time stepping for each adaptive grid level (or sub-cycling). Conservative flux correction at coarse-fine grid interfaces [19] is implemented for any kind of conservative fluxes in the telescoping form. The 13-point fourth-order dispersion-relation-preserving (DRP) scheme by Bogey and Bailly [20] that is re-cast in the conservative flux difference form [15, 21] is used for the discretization of the convective flux. Explicit tenth-order finite difference schemes are used to discretize the diffusive and viscous terms as source terms of the equations. An adjustable sponge buffer zone is implemented at the domain boundaries (both faces in the x-direction) to remove outgoing waves at the boundaries smoothly such that the wave reflection at the boundaries is kept at a minimal level. A third-order total variation diminishing Runge–Kutta (RK-TVD) scheme [22] is adopted for time integration with the local time stepping for each grid level. The Structured Adaptive Mesh Refinement Application Infrastructure (SAMRAI) [23–27] library from Lawrence Livermore National Laboratory (LLNL) is utilized for the parallelization of the code and the management of adaptive grids. Feature-based sensors are implemented to identify regions of interest for AMR. These include gradient and wavelet sensors [28] on different flow fields. A value sensor based on the mass fraction is used to identify mixing regions for grid refinement in this work. HAMeRS has been used successfully for the study of 2D multi-mode compressible two-layer RTI at a low Atwood number with the same DRP scheme [14] and three-dimensional (3D) multi-mode Richtmyer–Meshkov instability (RMI) at a high Atwood number [29, 30] with a shock-capturing scheme [31].

C. Problem Initialization

All cases investigated in this study are initialized with an isopycnic background stratification where the species densities of the involved fluids, ρ_i, are constant within the domain, and the hydro-static pressure field, p^H, can be determined by

$$\frac{dp^H(x)}{dx} = \rho^H g, \tag{26}$$

where ρ^H is the hydro-static mixture density. The domain considered in this study is $[-L_x/\lambda_0, L_x/\lambda_0] \times [0, L_y/\lambda_0]$, where $L_x = 10\lambda_0$ and $L_y = 16\lambda_0$. λ_0 is the characteristic wavelength of the multi-mode perturbation defined later. The middle layer is centered at $x/\lambda = 0$. The two interfaces are located at $x = \pm\Delta$ where Δ is the shift of the two interfaces from $x/\lambda = 0$. The interfaces at $x = -\Delta$ and $x = \Delta$ are called **first** (bottom) and **second** (top) interfaces in this work. In this study, we conduct DNS with different values of Δ to investigate the effects of the distance or initial middle layer width on the three-layer RTI flows. The two interfaces are initially diffuse by imposing error functions with

characteristic thickness, δ, on the initial hydro-static volume fractions of the three species, Z_i^H:

$$Z_1^H = \frac{1}{2} - \frac{1}{2}\,\mathrm{erf}\left(\frac{x+\Delta}{\delta}\right), \tag{27}$$

$$Z_2^H = \frac{1}{2}\,\mathrm{erf}\left(\frac{x+\Delta}{\delta}\right) - \frac{1}{2}\,\mathrm{erf}\left(\frac{x-\Delta}{\delta}\right), \tag{28}$$

$$Z_3^H = \frac{1}{2} + \frac{1}{2}\,\mathrm{erf}\left(\frac{x-\Delta}{\delta}\right). \tag{29}$$

Therefore, ρ^H is given by

$$\begin{aligned}\rho^H &= \rho_1^H Z_1^H + \rho_2^H Z_2^H + \rho_3^H Z_3^H \\ &= \frac{1}{2}\left(\rho_1^H + \rho_3^H\right) + \frac{1}{2}\left(\rho_2^H - \rho_1^H\right)\mathrm{erf}\left(\frac{x+\Delta}{\delta}\right) + \frac{1}{2}\left(\rho_3^H - \rho_2^H\right)\mathrm{erf}\left(\frac{x-\Delta}{\delta}\right).\end{aligned} \tag{30}$$

Furthermore, p^H can be obtained by integrating Equation (26):

$$\begin{aligned}p^H - p_0 = &\frac{1}{2}\left(\rho_1^H + \rho_3^H\right) gx \\ &+ \frac{1}{2}\left(\rho_2^H - \rho_1^H\right) g\left\{-\Delta\,\mathrm{erf}\left(\frac{\Delta}{\delta}\right) + (x+\Delta)\,\mathrm{erf}\left(\frac{x+\Delta}{\delta}\right) + \frac{\delta}{\sqrt{\pi}}\left[\exp\left(-\frac{(x+\Delta)^2}{\delta^2}\right) - \exp\left(-\frac{\Delta^2}{\delta^2}\right)\right]\right\} \\ &+ \frac{1}{2}\left(\rho_3^H - \rho_2^H\right) g\left\{-\Delta\,\mathrm{erf}\left(\frac{\Delta}{\delta}\right) + (x-\Delta)\,\mathrm{erf}\left(\frac{x-\Delta}{\delta}\right) + \frac{\delta}{\sqrt{\pi}}\left[\exp\left(-\frac{(x-\Delta)^2}{\delta^2}\right) - \exp\left(-\frac{\Delta^2}{\delta^2}\right)\right]\right\},\end{aligned} \tag{31}$$

where p_0 is the initial hydro-static pressure at $x/\lambda_0 = 0$.

Multi-mode perturbation with nine modes is used to perturb the initial volume fraction, Z_i, of the species at two different interfaces. The perturbed displacements in the x-direction, η^- and η^+, from the original interface locations are given by

$$\eta(y)^{\pm} = \frac{\eta_0}{3}\sum_{m=12}^{20}\left[\cos\left(\frac{2\pi m y}{L_y} + \phi_m^{\pm}\right)\right], \tag{32}$$

where m is the mode number and the middle mode number, m_d, is 16 in this work. The characteristic wavelength, λ_0, is defined as $\lambda_0 = L_y/m_d$. $\phi_m^{\pm} \in [0, 2\pi)$ are random phase shifts for each mode m at the two interfaces respectively at $x = \pm\Delta\lambda_0$. As a result, the perturbed volume fraction fields of the three fluids are given by

$$Z_1^H(x,y) = \frac{1}{2} - \frac{1}{2}\,\mathrm{erf}\left(\frac{x+\eta(y)^- + \Delta}{\delta}\right), \tag{33}$$

$$Z_2^H(x,y) = \frac{1}{2}\,\mathrm{erf}\left(\frac{x+\eta(y)^- + \Delta}{\delta}\right) - \frac{1}{2}\,\mathrm{erf}\left(\frac{x+\eta(y)^+ - \Delta}{\delta}\right), \tag{34}$$

$$Z_3^H(x,y) = \frac{1}{2} + \frac{1}{2}\,\mathrm{erf}\left(\frac{x+\eta(y)^+ - \Delta}{\delta}\right). \tag{35}$$

The characteristic initial thickness of the interface δ is set to be 4% of λ_0 for all cases in this work.

In addition to the Atwood number, there are two more important non-dimensional quantities to characterize the compressible RTI [14, 32]. The first one is the isothermal Mach number, Ma_0, that characterizes the background stratification strength, which is defined as

$$Ma_0 = \frac{\sqrt{g\lambda_0}}{c_0}, \tag{36}$$

where c_0 is the isothermal speed of sound at $x/\lambda_0 = 0$. In addition, the problem Reynolds number, Re_0, is defined as:

$$Re_0 = \sqrt{\frac{g\lambda_0^3}{\nu_0^2}}. \tag{37}$$

As the focus of this study is investigating three-species mixing with different stratification scenarios at the second (upper) interface, Ma_0 is approximately the same at around 0.15 (see Table 1) and Re_0 is kept constant at 3000 for all cases.

Case	Δ	A_0	A_1	A_2	M_1/M_2	M_2/M_3	M_1/M_3	Ma_0
HIL_1	$\lambda_0/4$	0.0400	0.0196	0.0204	1.0400	1.0417	1.0833	0.1500
HIL_2	$\lambda_0/2$	0.0400	0.0196	0.0204	1.0400	1.0417	1.0833	0.1500
HLL_1	$\lambda_0/4$	0.0400	0.0400	0.0000	1.0833	1.0000	1.0833	0.1470
HLL_2	$\lambda_0/2$	0.0400	0.0400	0.0000	1.0833	1.0000	1.0833	0.1470
HLI_1	$\lambda_0/4$	0.0400	0.0400	−0.0204	1.0833	0.9600	1.0400	0.1470
HLI_2	$\lambda_0/2$	0.0400	0.0400	−0.0204	1.0833	0.9600	1.0400	0.1470
HLH_1	$\lambda_0/4$	0.0400	0.0400	−0.0400	1.0833	0.9231	1.0000	0.1470
HLH_2	$\lambda_0/2$	0.0400	0.0400	−0.0400	1.0833	0.9231	1.0000	0.1470

Table 1 Details of the investigated DNS cases. HIL: Heavy-Intermediate-Light densities; HLL: Heavy-Light-Light densities; HLI: Heavy-Light-Intermediate densities; HLH: Heavy-Light-Heavy densities. The subscripts of 1 and 2 after the representative three letters represent the shorter ($\lambda_0/4$) and longer ($\lambda_0/2$) distances between fluids 1 and 3, respectively.

D. Simulation Cases

In this work, we have designed four different stratification cases with two different values for Δ to study the three-layer RTI using DNS. Table 1 presents the important non-dimensional parameters used in these cases. Four stratification scenarios are designed to compare the effects of the Atwood numbers at the two interfaces on the RTI growth at both interfaces for two different Δ values, $\Delta = \lambda_0/4$ and $\Delta = \lambda_0/2$. For all eight cases, the global Atwood number A_0 is kept at 0.04 (see Equation (2)). This corresponds to the ratio of heaviest to lightest molecular weights, M_H/M_L, of 1.0833. When the species all have different molecular weights, the molecular weight of the intermediate species is the mean of the heaviest and lightest molecular weights of the species. As a result, the ratio of the intermediate weight, M_I, to the lightest molecular weight, M_L, is given by

$$\frac{M_I}{M_L} = \frac{1}{2}\left(1 + \frac{M_H}{M_L}\right). \tag{38}$$

Since M_H/M_L is 1.0833, M_I/M_L (M_L/M_I) is 1.0417 (0.9600). Here, values larger than unity represent unstable interfaces. In the cases of Heavy-Intermediate-Light (HIL_1 and HIL_2) densities, the stratification of the fluids generates two unstably stratified interfaces with local Atwood numbers, $A_1 = 0.0196$ and $A_2 = 0.0204$. In addition, since fluid 2 at $x/\lambda_0 = 0$ has intermediate molecular mass, M_I, for the Heavy-Intermediate-Light (HIL_1 and HIL_2) stratification cases, the corresponding Ma_0 is slightly different for the HIL, compared to HLL, HLI, and HLH cases whose fluid 2 is the lightest fluid with M_L (see Equation (36)).

The corresponding Atwood number at different interfaces of the different cases gets the following values. For the Heavy-Light-Light (HLL), Heavy-Light-Intermediate (HLI), and Heavy-Light-Heavy (HLH) cases, the fluids from bottom to top (negative to positive x-direction) have heavy-light-light, heavy-light-intermediate and heavy-light-heavy densities, respectively. Hence, all cases have $A_0 = A_1 = 0.04$ whereas the HLL has $A_2 = 0$, HLI has $A_2 = -0.0204$, and both cases indicate a globally unstable case as $M_1 > M_3$ and HLH has $A_2 = -0.04$ representing globally neutrally stratified case as $M_1 = M_3$. For the HLL cases, we note that although fluids 2 and 3 have identical material properties, including having the same molecular weights, we treat them as separate fluids that allow us to track their mass fractions and compare them with other cases under different stratification scenarios.

III. Results and Discussions

A. Visualizations of Density, Mass Fraction, and Vorticity at Different Times

First, we study the qualitative differences between the investigated cases by showing 2D contours of the mass fraction, density, and vorticity fields at different time instants. The mass fraction and density contours show the large-scale motions, such as the fluid entrainment of the RTI flows, while the vorticity plots display the development of the small scales in the flows.

Figure 2 presents the density field for the four cases with $\Delta = \lambda_0/2$ at different non-dimensional time instants, t^*, where time scale, $t_r = \sqrt{\lambda_0/g}$, is used for the non-dimensionalization of time, i.e., $t^* = t/t_r$. At $t^* = 10$, three layers are

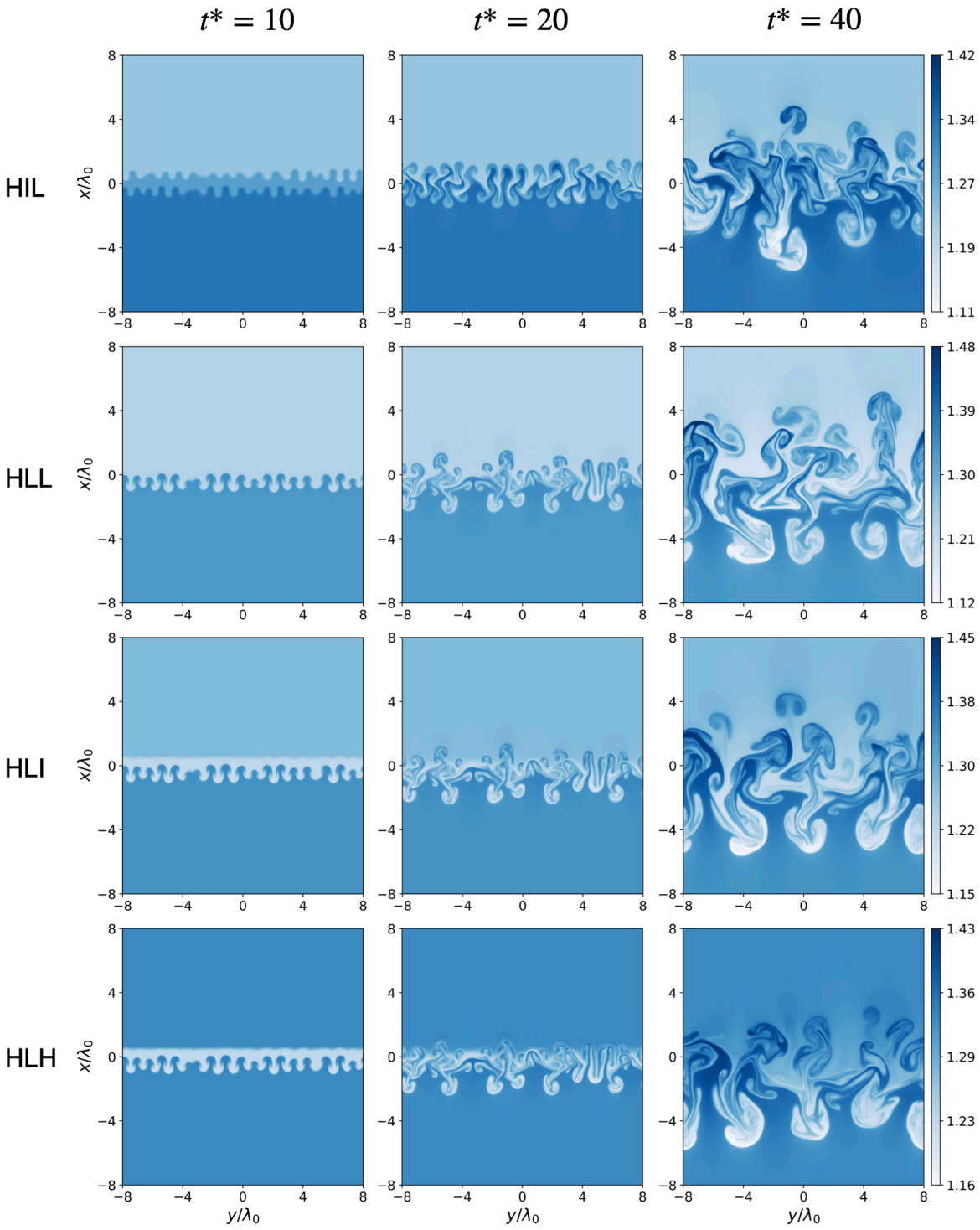

Fig. 2 Evolution of the density field for the HIL_2, HLL_2, HLI_2, and HLH_2 cases from top to bottom column, respectively. Non-dimensional times from left to right are $t^* = 10,\ 20,$ and 40. The vertical axis is the x-direction, and the acceleration points upward.

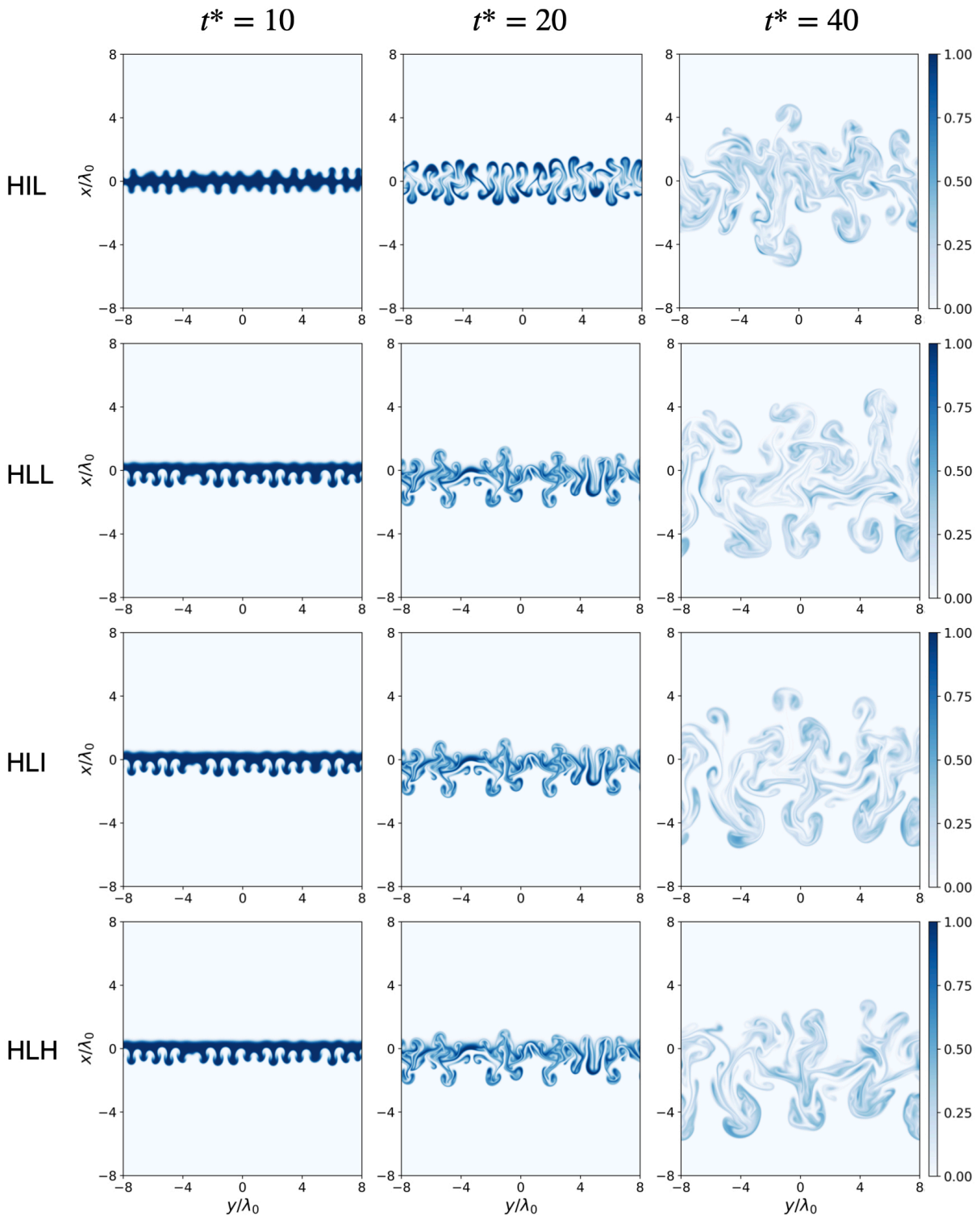

Fig. 3 Evolution of the mass fraction of fluid 2 for the HIL_2, HLL_2, HLI_2, and HLH_2 cases from top to bottom columns, respectively. Non-dimensional times from left to right are $t^* = 10,\ 20,$ and 40. The vertical axis is the x-direction, and the acceleration points upward.

still distinguishable as fluids 1 and 3 are not interacting yet for the HIL_2, HLI_2, and HLH_2 cases. For the HLL_2 case, as fluids 2 and 3 are essentially the same fluid, the third layer is not visible, and we only observe the first (bottom) interface. In addition, the density field evolution shows that the penetration of the middle fluid (fluid 2) is symmetric for the HIL_2 case at $t^* = 10$. For this case, the presence of fluid 2 virtually disappears as the heaviest fluid interacts with the lightest fluid directly at later times $t^* > 20$, and the flow becomes similar to the classical two-layer RTI flow. The second interface is neutrally stable, weakly stable, and strongly stable for the rest of the cases, HLL_2, HLI_2 and HLH_2, respectively. Hence, there is no growth observed at the second (top) interface, and the penetration of fluid 2 becomes asymmetric as it only moves downwards, and the initial perturbations smooth out at the second (top) interface due to molecular diffusion and stabilization for the cases HLI_2 and HLH_2. At a later time $t^* > 20$, when fluid 1, or the first (bottom) interface, reaches the second (top) interface, the former disturbs the latter and penetrates into the pure fluid region of fluid 3. As a result, fluid 3 starts moving downwards as well due to the fluid entrainment. However, the growth rate of the second (upper) interface shows some sensitivity to the background stratification strength as the RTI growth rate in the upward direction for the HLI_2 case is slower than that of the HLL_2 case. We would also like to highlight that the upward growth rate of the RTI mixing layer is slowest for the HLH_2 case, however, it does not stop growing even though the second (top) interface is initially strongly stable. This is attributed to the inertia of the heavy fluid 1 that continues to move in the upward direction. In addition, although both fluids 1 and 3 have the same molar masses, the density of fluid 1 stays continuously larger than fluid 3 when they are at the same height (at the same x/λ_0), and this, in fact, further feeds the growth.

Figure 3 presents the mass fraction of the middle fluid (fluid 2), Y_2, for the HIL_2, HLL_2, HLI_2, and HLH_2 cases at different non-dimensional time instants. First, it should be noted again that fluids 2 and 3 are the same fluid for the HLL case. However, treating them as separate species allows us to follow the evolution of Y_2 for comparison purposes. At early time, $t^* = 10$, the fluid 2 moves in the positive and negative x-directions to generate spikes and bubbles in the two different directions, respectively, for the HIL case as both interfaces are RT unstable. On the other hand, the motion of fluid 2 in the other three cases (HLI, HLH, and HLL) dominantly moves in the negative direction as bubbles because the second (top) interfaces between fluids 2 and 3 of these cases are either stably or neutrally stratified. At the same time, fluid 1 also migrates upward at the first (bottom) interface to form spikes. At $t^* = 20$, the penetration of fluid 2 continues in both directions for the HIL case. The growth of bubbles/spikes becomes more chaotic at the same time while the upward and downward penetrating motions stay symmetric qualitatively. Here, symmetry refers to similar fluid penetrations of fluid 2 into fluids in the negative and positive x-directions. For the HLL, HLI, and HLH cases, the spikes and bubbles at the first (bottom) interface between fluids 1 and 2 continuously grow and the second (top) interface is disturbed to form spikes and bubbles too. However, the growth of the spikes and bubbles at the second (top) interface is slower as fluid 3 is either a denser fluid or fluid of the same density (basically the same fluid). The vortical motions at the second (top) interface (between fluids 2 and 3) are less chaotic compared to those at the first (bottom) interface (between fluids 1 and 2) for these three cases compared to case HIL but the effect of A_2 is not noticeable at $t^* = 20$ among these three cases. At $t^* = 40$, the growth of spikes and bubbles remains symmetric for the HIL case. In addition, due to the stronger stratification at the second (top) interface, the growth of the bubbles at the second (top) interface is slower for the HLH case compared to the HLL and HLI cases. The lighter blue color at $t^* = 40$ indicates that fluid 2 is quite thoroughly mixed with fluids 1 and 3, and we do not observe pure fluid 2 (with dark blue color) within the domain anymore.

Figure 4 presents the effects of the initial distance between the first (bottom) and second (top) interfaces, $2 \times \Delta$, on the mass fraction of fluid 2, Y_2, at $t^* = 40$ for the HLI case. As the case with larger Δ initially has a larger amount of fluid 2, the Y_2 plot has darker blue regions for the HIL_2 case compared to HIL_1 at the same time instant. In addition, there are small structural differences between cases HIL_1 and HIL_2, which is attributed to the delayed interaction of fluids 1 and 3 because of the presence of an initially thicker fluid 2 layer for the HIL_2 case. A more quantitative comparison of the growth of mixing layer widths is presented in the next section. Figure 5 compares the contours of Y_2 for the HLL_1 and HLL_2 cases at $t^* = 40$ for the completeness of the analysis. There are no structural differences between the HLL_1 and HLL_2 cases as the second (upper) interface of these two cases actually does not exist since fluid 2 is identical to fluid 3. The maximum value, or the magnitude of Y_2 at $t^* = 40$ is smaller (seen as a lighter blue color in the plot) for the case HLL_1 compared to case HLL_2. This is due to the fact that the case HLL_1 initially has less amount of fluid 2, thus this smaller amount of pure fluid 2 is mixed at a faster rate with fluid 3. However, it should be clarified again that fluids 2 and 3 are basically the same species so the only difference between cases HLL_1 and HLL_2 is the initial location of the first (bottom) interface.

Next, we discuss the development of the vorticity, $\boldsymbol{\omega}$, which is defined as $\boldsymbol{\omega} = \nabla \times \boldsymbol{u}$. Figure 6 presents $\boldsymbol{\omega}$ normalized with t_r, for the four cases at $t^* = 5$. For the case HIL_2, since it has two unstable RTI interfaces, vortices are generated

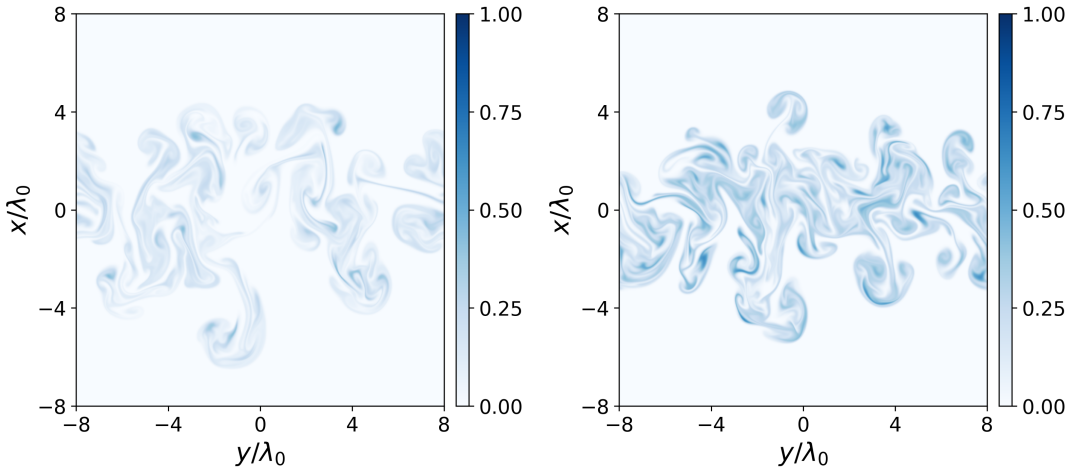

(a) HIL_1 (b) HIL_2

Fig. 4 Mass fraction of fluid 2 at $t^* = 40$ for the HIL cases with $\Delta = \lambda_0/4$ and $\Delta = \lambda_0/2$. The vertical axis is the x-direction, and the acceleration points upward.

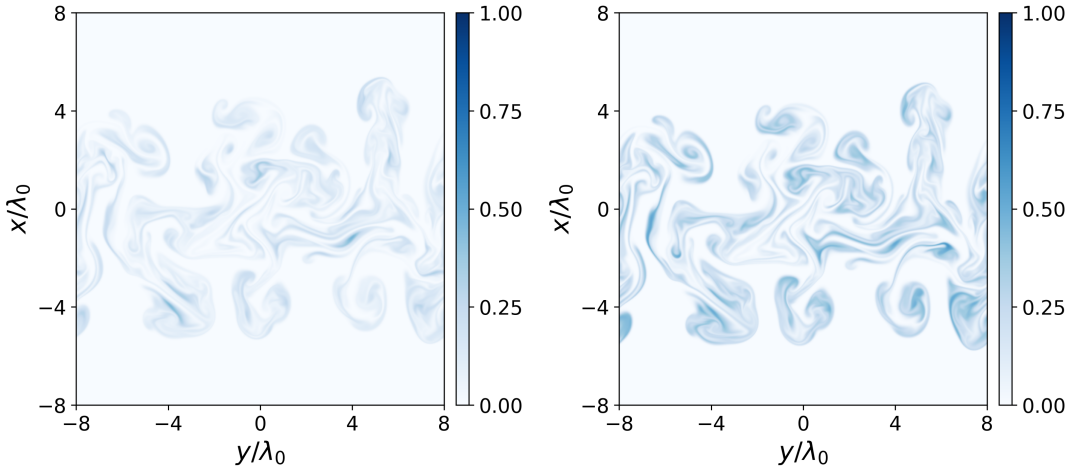

(a) HLL_1 (b) HLL_2

Fig. 5 Mass fraction of fluid 2 at $t^* = 40$ for the HLL cases with $\Delta = \lambda_0/4$ and $\Delta = \lambda_0/2$. The vertical axis is the x-direction, and the acceleration points upward.

at both interfaces due to the baroclinic production, or the misalignment of the density and pressure gradients. However, the production of vortices is only observed at the first (bottom) interface for the case HLL_2 as there is no density gradient between fluids 2 and 3 ($M_2 = M_3$) for this case. HLI_2 and HLH_2 cases have vortical motions at both interfaces as they both experience density gradients ($M_1 \neq M_2 \neq M_3$), but the magnitudes of the vorticity at the second (top) interface are significantly smaller than that of case HIL_2 as this interface is initially stably stratified ($M_2 < M_3$) for both cases. In addition, the HLL_2, HLI_2, and HLH_2 cases all generate stronger vortices at the first (bottom) interface compared to the case HIL_2 as $A_1 = 0.04$ for these three cases, but $A_1 = 0.0196$ for the HIL_2 case. Figure 7 presents the normalized ω at $t^* = 15$. Similar to the earlier time, HIL_2 case exhibits two unstable interfaces with two layers of vortical structures. It is important to note that both the first (bottom) and second (top) interfaces generate slightly different vortical structures since both interfaces have different random phase shifts in Equation (32) for the random initial perturbations at the interfaces. The effects of neutrally and stably stratified second (top) interface become more visible at this time instant as HLL_2, HLI_2, and HLH_2 cases have only one layer of vortical structures left that

is centered at $x/\lambda_0 \approx -\Delta$. Consistent with the previous time instant, these cases also generate stronger vortices and more chaotic flows around the first (bottom) interface than case HIL_2 as they have large values of A_1 compared to case HIL_2. Finally, we present ω at $t^* = 30$ in Figure 8. At this time, fluid 1 has already reached the regions initially occupied by fluid 3 for all cases. As a result, we see that there is virtually only one RTI mixing layer left which grows in both upward and downward directions. However, we also notice that when A_2 decreases (more negative), the vortices are weaker on the side of fluid 3, and there is less penetration of fluid 1 into fluid 3 due to a stronger stability effect.

B. Time Evolution of Mixing Quantities

The time evolution of the large-scale characteristic lengths of the RTI mixing are investigated with the integral mixing width of each fluid separately. It is defined for the i-th species as

$$W_i = 4 \int \overline{Y_i}(1 - \overline{Y_i})\, dx, \tag{39}$$

where $\overline{\cdot}$ represents the averaging in all homogeneous directions, i.e., y-direction in this work. The mixing widths are all normalized with λ_0.

Figure 9 presents the normalized mixing width of fluid 1, W_1/λ_0, for all cases under investigation. At early times ($t^* < 12$) for the case HIL with the two different values of Δ, the growth of mixing width of fluid 1 is also slower compared to the other cases as it has a smaller A_1. In addition, the growth of W_1/λ_0 is similar for the HLL, HIL, and HLH cases until the effect of the second (top) interface kicks in, which is at $t^* \approx 12$ for the cases with $\Delta = \lambda_0/4$ and at $t^* \approx 18$ for the cases with $\Delta = \lambda_0/2$. At late times, W_1/λ_0 of the case HIL_1 grows faster because the second (top) interface is unstable and eventually behaves like the HLL case, which is essentially a classical two-layer RTI flow. Figure 10 presents the normalized mixing width of fluid 2, W_2/λ_0. The evolution of W_2 is similar for all cases when the value of Δ is the same. It tends asymptotically to two different constant values for the cases with $\Delta = \lambda_0/4$ and $\Delta = \lambda_0/2$ respectively. Because there is a finite amount of fluid 2 within the domain, while fluid 2 continues to penetrate downward and upward within the domain, it mixes with fluids 1 and 3 which leads to a saturation for the growth of W_2. The growth of the normalized mixing width of fluid 3, W_3/λ_0, is shown in Figure 11. It can be seen that the growth of this width starts earlier for the HIL case compared to other cases (HLL, HLI, and HLH) since the second (top) interface is only unstably stratified for the HIL case. As a result, the two interfaces interact with each other earlier for this case.

The molecular mixing between any pair of species i and j can be measured using the mixing metric:

$$\Psi_{ij} = \frac{\int \overline{Y_i Y_j}\, dx}{\lambda_0}, \tag{40}$$

which is basically the domain integration of the product of mass fractions of the two species, normalized with the domain width, L_y, and the perturbation characteristic length, λ_0. Particularly, Ψ_{13} provides critical information as the zero value of Ψ_{13} indicates that fluids 1 and 3 have not interacted with each other yet, while $\Psi_{13} > 0$ indicates some level of interaction between fluids 1 and 3.

Figure 13 presents the time evolution of Ψ_{13} for different cases. It can be seen that Ψ_{13} is initially zero for all cases because of the existence of the pure fluid 2 layer that separates fluids 1 and 3. At later times, Ψ_{13} starts increasing as fluids 1 and 3 reach each other and the mixing between them starts. To determine a time instant when fluids 1 and 3 start interacting with each other, we use a value of $\Psi_{13} = 0.01$ as a threshold. In Figure 13, the vertical black solid and red dash-dotted lines represent the normalized time instants when fluids 1 and 3 start interacting with each other for the cases with $\Delta = \lambda_0/4$ and $\Delta = \lambda_0/2$, respectively. Using a threshold of $\Psi_{13} = 0.01$, the normalized times when mixing between fluids 1 and 3 begin for the cases HIL_1, HLL_1, HLI_1, HLH_1, HIL_2, HLL_2, HLI_2, and HLH_2 are 15.2, 12.6, 12.6, 12.8, 18.8, 19.2, 19.4, and 19.4, respectively. As can be anticipated, when the initial distance between the two interfaces, $2 \times \Delta$, increases, the interaction time between fluids 1 and 3 delays. Comparing HIL cases with the HLL, HLI, and HLH cases using the same value of Δ, fluid 1 reaches fluid 3 at later times for the former cases as the effective Atwood number at the first (bottom) interface, A_1, is smaller, so the RTI mixing layer growth of the interface is slower at earlier times. On the other hand, the stratification strength at the second (top) interface has a limited effect on the normalized time instant of interaction between fluids 1 and 3, which can be seen for HLL, HLI, and HLH cases with the same value of Δ.

The mixedness parameter, Θ_i, of the i-th species is defined as

$$\Theta_i = \frac{\int \overline{Y_i\ (1 - Y_i)}\, dx}{\int \overline{Y}_i\ \overline{(1 - Y_i)}\, dx}, \tag{41}$$

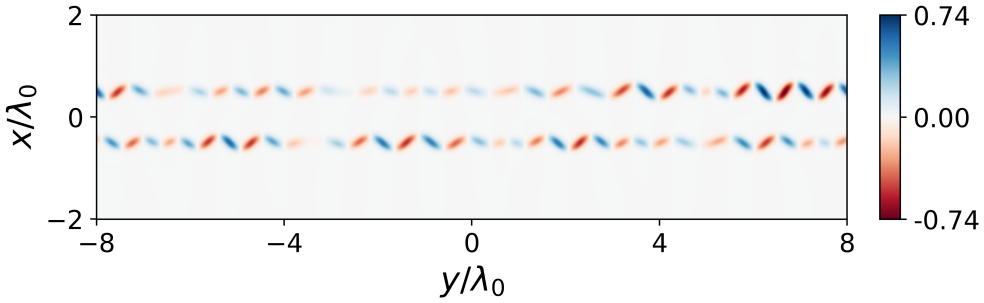

(a) t^* = 5, HIL_2

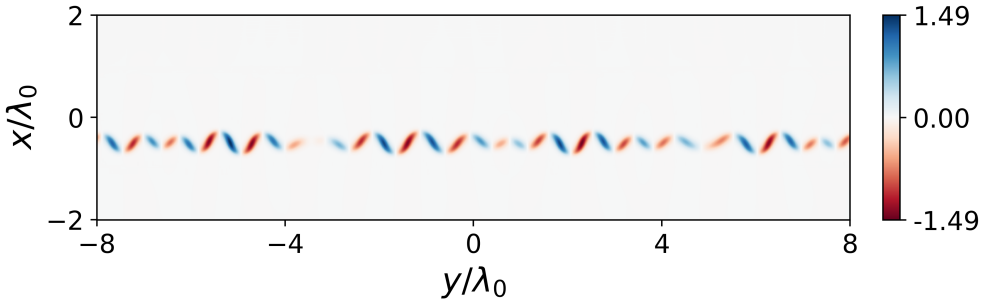

(b) t^* = 5, HLL_2

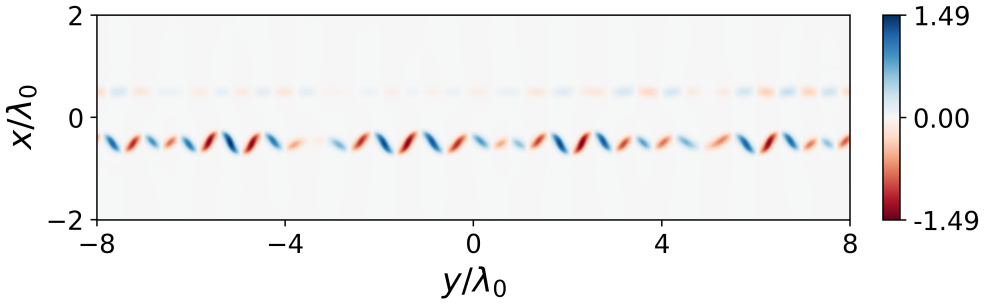

(c) t^* = 5, HLI_2

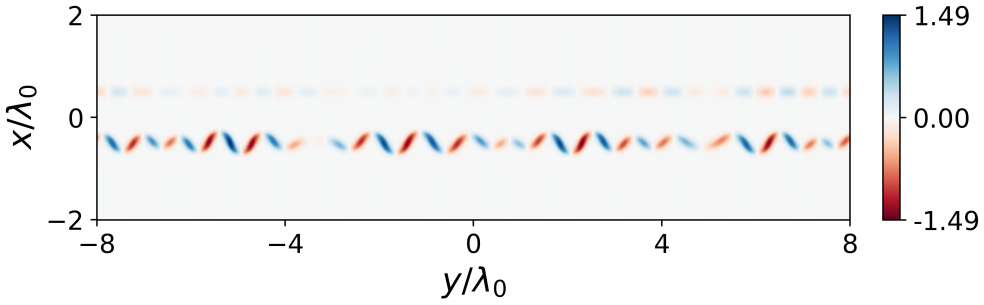

(d) t^* = 5, HLH_2

Fig. 6 Vorticity normalized with t_r at $t^* = 5$ for the HIL_2, HLL_2, HLI_2, and HLH_2 cases. The vertical axis is the x-direction, and the acceleration points upward.

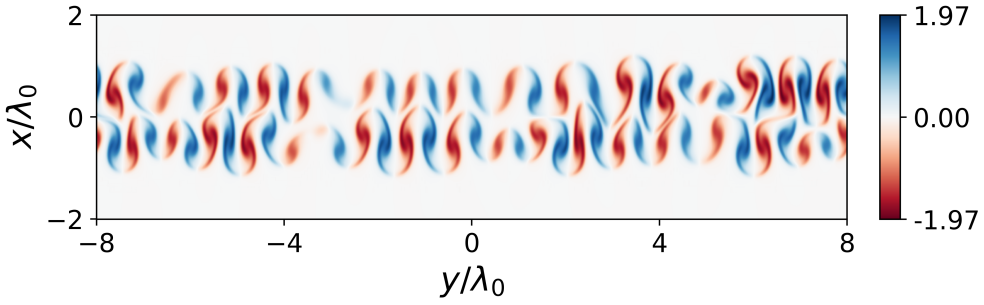

(a) t^* = 15, HIL_2

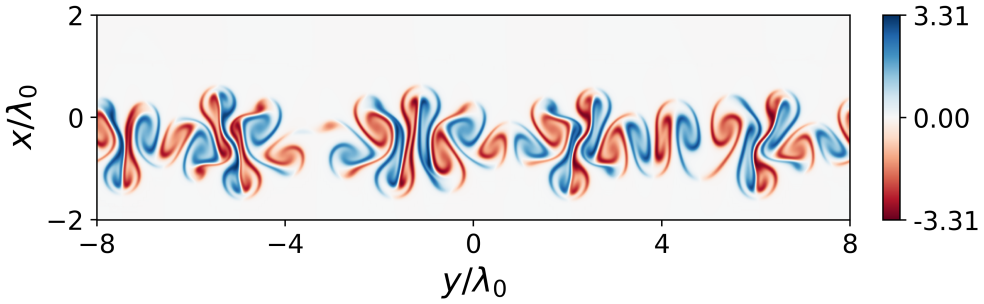

(b) t^* = 15, HLL_2

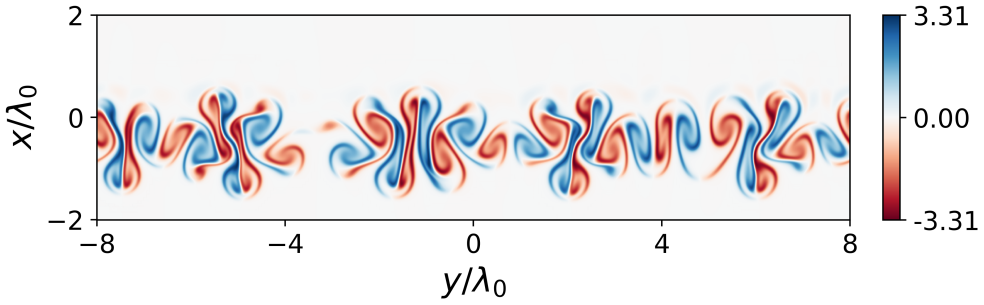

(c) t^* = 15, HLI_2

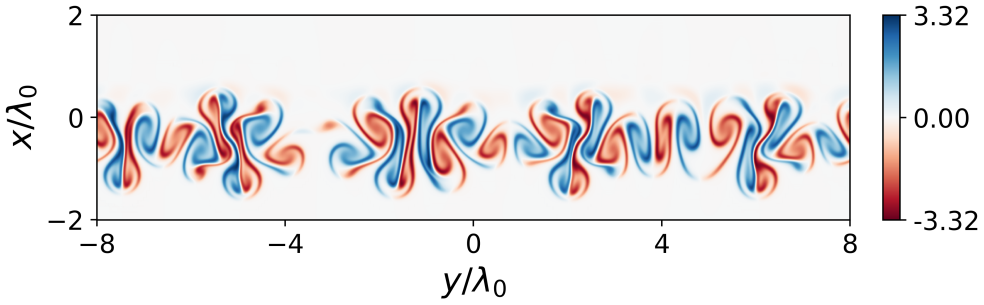

(d) t^* = 15, HLH_2

Fig. 7 Vorticity normalized with t_r at t^* = 15 for the HIL_2, HLL_2, HLI_2, and HLH_2 cases. The vertical axis is the x-direction, and the acceleration points upward.

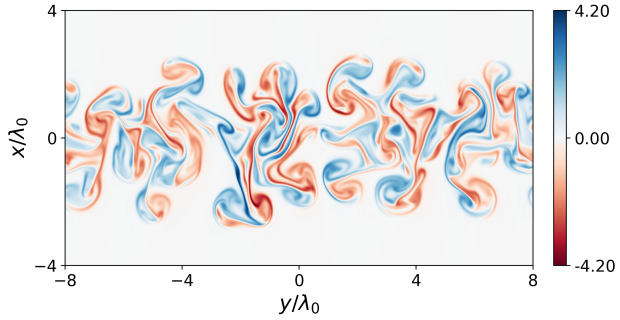

(a) t^* = 30, HIL_2

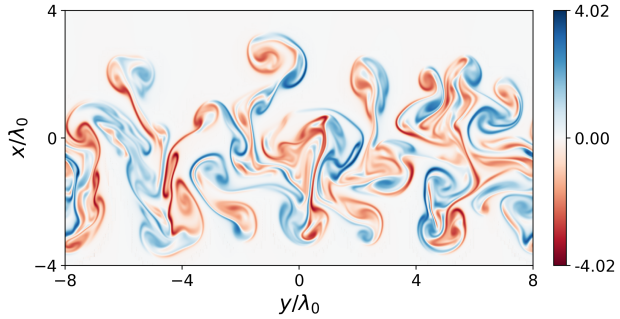

(b) t^* = 30, HLL_2

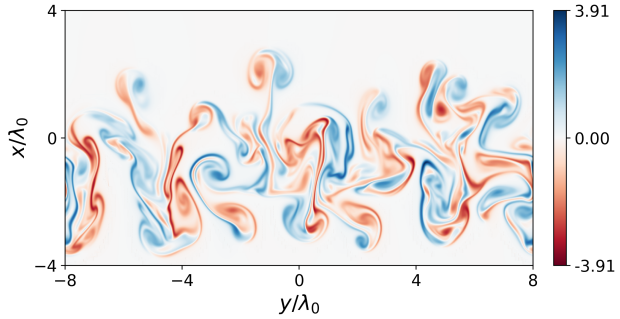

(c) t^* = 30, HLI_2

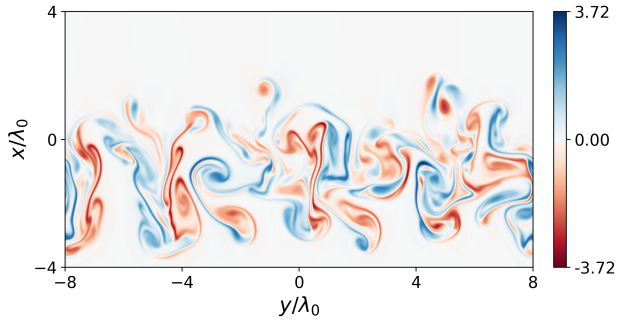

(d) t^* = 30, HLH_2

Fig. 8 Vorticity normalized with t_r at t^* = 30 for the HIL_2, HLL_2, HLI_2, and HLH_2 cases. The vertical axis is the x-direction, and the acceleration points upward.

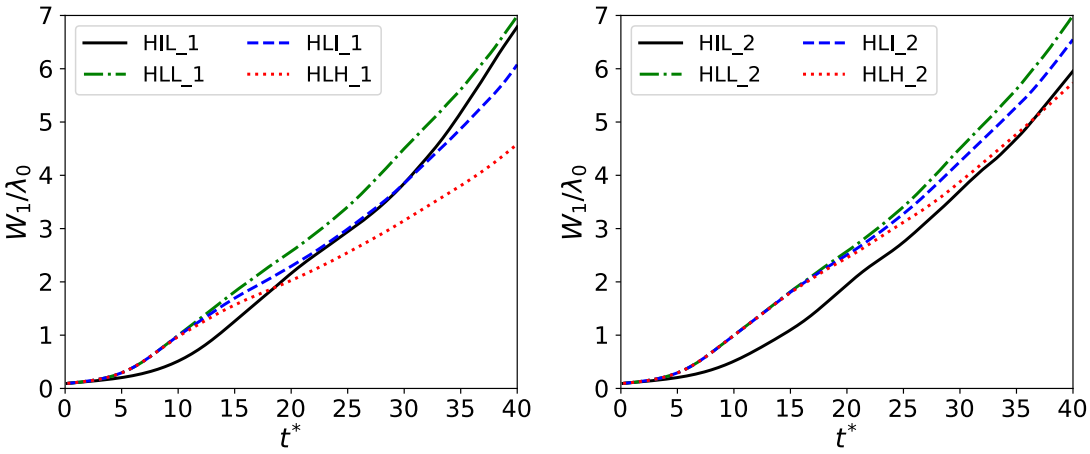

(a) $W_1/\lambda_0, \Delta = \lambda_0/4$ (b) $W_1/\lambda_0, \Delta = \lambda_0/2$

Fig. 9 Time evolution of the normalized mixing width of fluid 1 (W_1/λ_0) for different cases with $\Delta = \lambda_0/4$ and $\Delta = \lambda_0/2$. Black solid line: HIL; green dash-dotted line: HLL; blue dashed line: HLI; red dotted line: HLH.

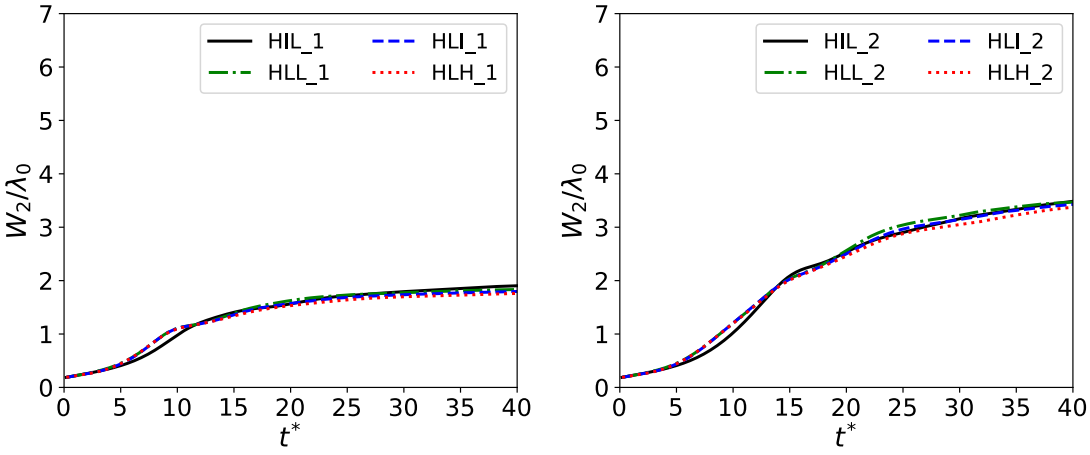

(a) $W_2/\lambda_0, \Delta = \lambda_0/4$ (b) $W_2/\lambda_0, \Delta = \lambda_0/2$

Fig. 10 Time evolution of the normalized mixing width of fluid 2 (W_2/λ_0) for different cases with $\Delta = \lambda_0/4$ and $\Delta = \lambda_0/2$. Black solid line: HIL; green dash-dotted line: HLL; blue dashed line: HLI; red dotted line: HLH.

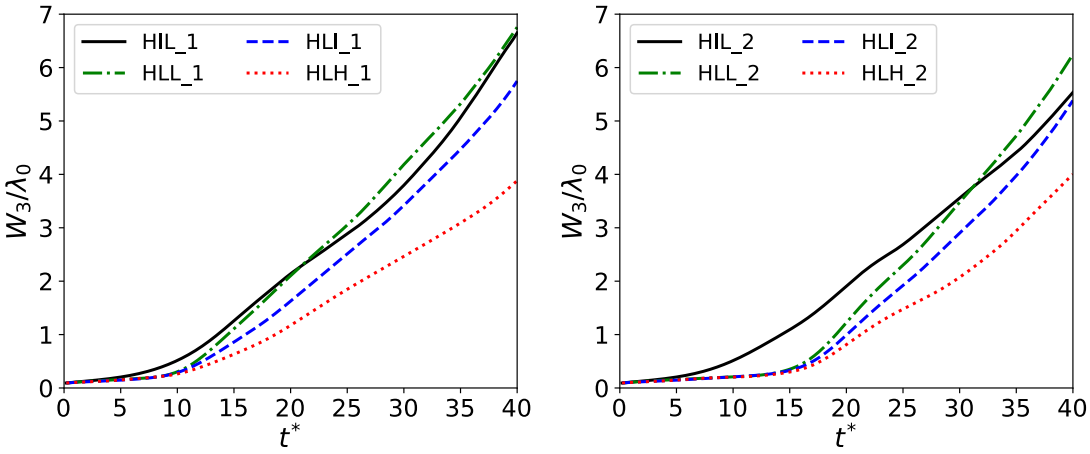

(a) $W_3/\lambda_0, \Delta = \lambda_0/4$ (b) $W_3/\lambda_0, \Delta = \lambda_0/2$

Fig. 11 Time evolution of the normalized mixing width of fluid 3 (W_3/λ_0) for different cases with $\Delta = \lambda_0/4$ and $\Delta = \lambda_0/2$. Black solid line: HIL; green dash-dotted line: HLL; blue dashed line: HLI; red dotted line: HLH.

which has a value between zero and unity for the situation from an unmixed to a fully mixed mixing layer, respectively. This quantity can also be thought as an estimation of the amount of the i-th species molecularly mixed with other species within the corresponding mixing layer [29]. Θ_i of each fluid for all investigated cases with the two different values of Δ are compared in Figure 14. From the figure, it can be seen that Θ_1 increases at very early times due to molecular mixing for all cases. However, when the RTI instability grows, its value decreases due to the larger entrainment of pure fluids into the mixing layer between fluids 1 and 2 for each case. The decrease in Θ_1 for the HIL cases, independent of the value of Δ, happens at later times compared to other cases, due to smaller Atwood number (weaker stratification) at the first (bottom) interface (not shown here for brevity).

Figure 15 presents the effect of Δ on Θ_2 for each case. These plots show that initially, the growth of Θ_2 follows the same path for each case, where there is an increase in its value at very early times due to the molecular diffusion followed by a drop because of the RTI-induced fluid entrainment at the first (bottom) interface, no matter what the value of Δ is. However, there is a delay in the second increasing stage of Θ_2 when the cases with $\Delta = \lambda_0/2$ is compared to the cases with $\Delta = \lambda_0/4$ due to the larger region of pure fluid 2 in the entire RTI system initially for the former cases. These results show consistency with the time evolution of Y_2 discussed in the previous section.

The time evolution of Θ_3 is largely affected by the Atwood number at the second (top) interface at early times (see both Figures 14(e) and 14(f)). Fluid 3 of the HLI and HLH cases is molecularly well mixed at the second (top) interface at early times since the second (top) interface is not RT unstable for these cases, and perturbation is removed by both stabilization and molecular diffusion effects. On the other hand, for the HLL cases, Θ_3 does not increase to unity as quickly as the HLI and HLH cases. This is due to the fact that, in this case, there are no density gradients between fluids 2 and 3 since both fluids are the same, so the only mechanism is diffusion that initially increases the value of Θ_3. At later times, when the second (top) interface is disturbed by the first (bottom) interface, Θ_3 decreases again as the momentum of the first (bottom) interface leads to fluid entrainment between fluid 3 and another two fluids. When $\Delta = \lambda_0/4$, Θ_3 approaches very similar values for all cases at the end of simulations. However, the effect of the initial stratification on Θ_3 at very late times is larger for the cases with $\Delta = \lambda_0/2$. At very late times, fluid 3 is more molecularly mixed for case HIL_2, compared to the HLL_2, HIL_2, and HLH_2 cases.

Figure 16 presents the effect of Δ on Θ_3 for each case with the two different values of Δ. While the effect of Δ on Θ_3 is small for the HIL cases, its effect is much larger for the HLL, HIL, and HLH cases where the drop in the value of Θ_3 is delayed when Δ is larger. When Δ is increased, there is a larger distance between the two interfaces. Therefore, the second (top) interface is disturbed by the first (bottom) interface at a later time for the entrainment of fluid 3 with other fluids to happen.

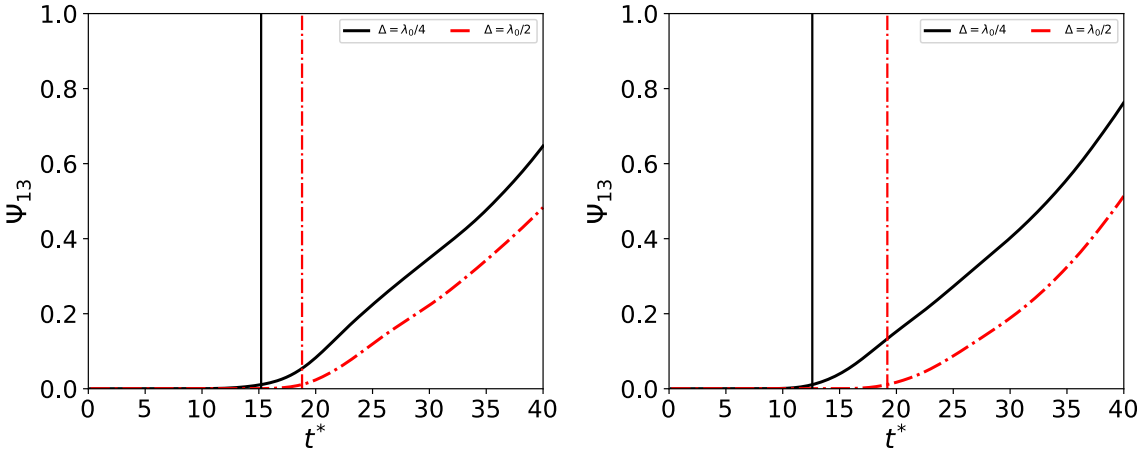

(a) HIL

(b) HLL

(c) HLI

(d) HLH

Fig. 12 Time evolution of mixing metric between fluids 1 and 3, Ψ_{13}, for different cases with different values of Δ. Black solid line: $\Delta = \lambda_0/4$; red dash-dotted line: $\Delta = \lambda_0/2$. The vertical lines indicate the normalized times when the threshold $\Psi_{13} = 0.01$ is reached for the corresponding cases.

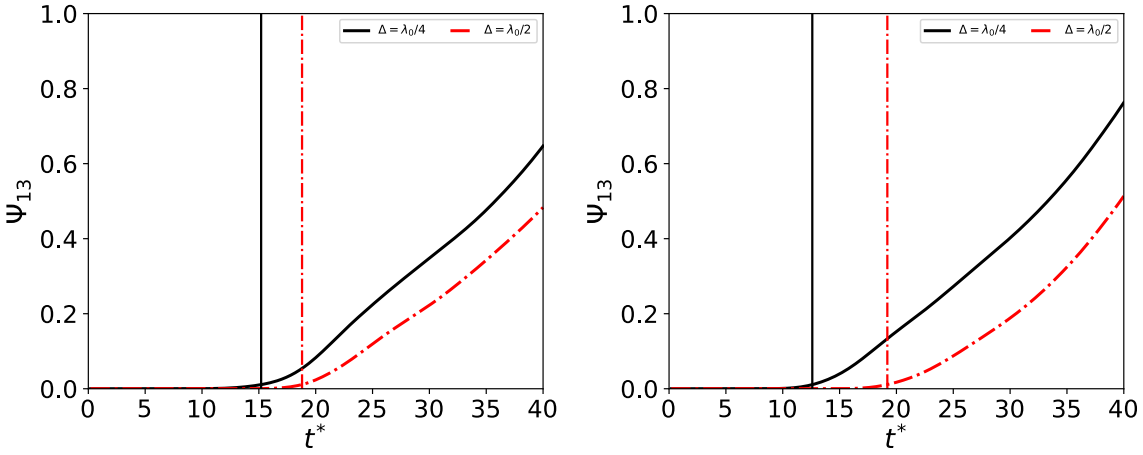

(a) HIL

(b) HLL

(c) HLI

(d) HLH

Fig. 13 Time evolution of mixing metric between fluids 1 and 3, Ψ_{13}, for different cases with different values of Δ. Black solid line: $\Delta = \lambda_0/4$; red dash-dotted line: $\Delta = \lambda_0/2$. The vertical lines indicate the normalized times when the threshold $\Psi_{13} = 0.01$ is reached for the corresponding cases.

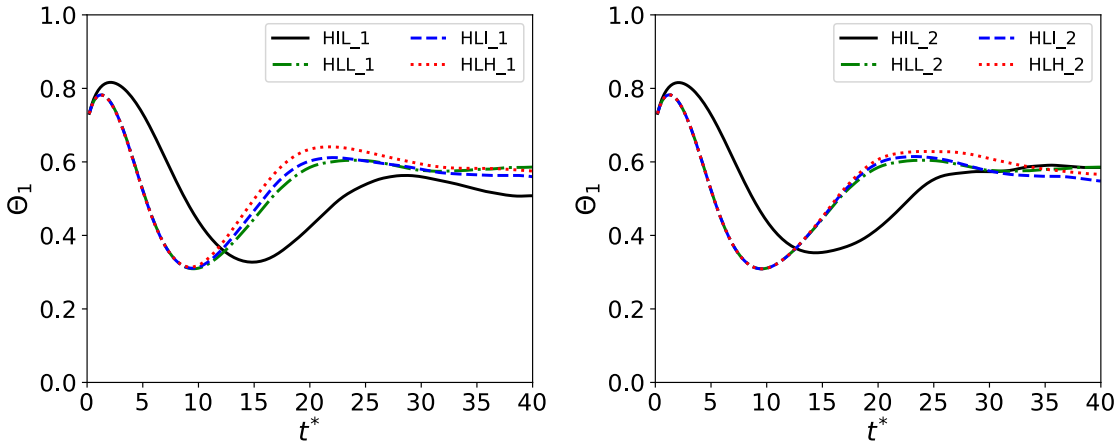

(a) Θ_1, $\Delta = \lambda_0/4$

(b) Θ_1, $\Delta = \lambda_0/2$

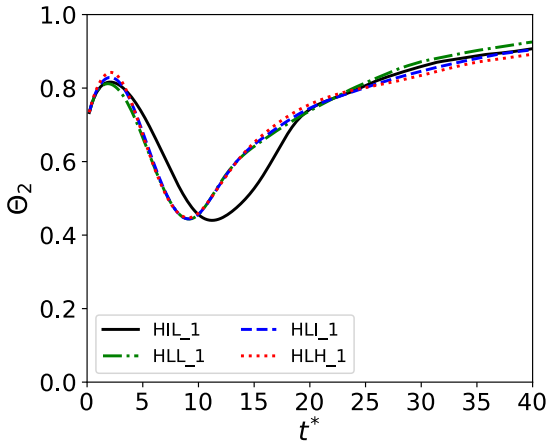

(c) Θ_2, $\Delta = \lambda_0/4$

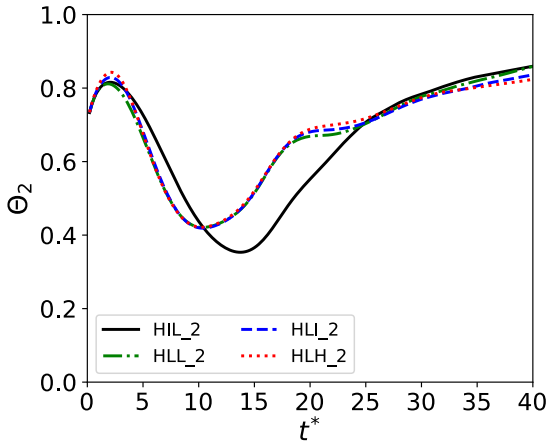

(d) Θ_2, $\Delta = \lambda_0/2$

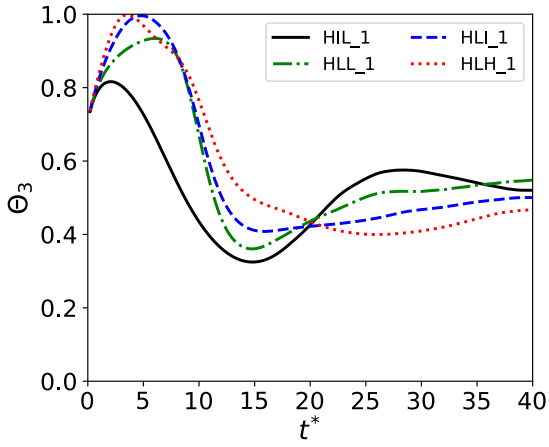

(e) Θ_3, $\Delta = \lambda_0/4$

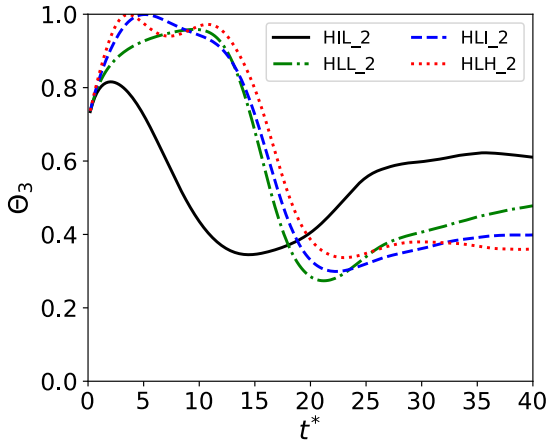

(f) Θ_3, $\Delta = \lambda_0/2$

Fig. 14 Time evolution of the mixedness, Θ_i, of fluid 1 (Θ_1), fluid 2 (Θ_2), and fluid 3 (Θ_3), from top to bottom, for different cases with $\Delta = \lambda_0/4$ and $\Delta = \lambda_0/2$. Black solid line: HIL; green dash-dotted line: HLL; blue dashed line: HLI; red dotted line: HLH.

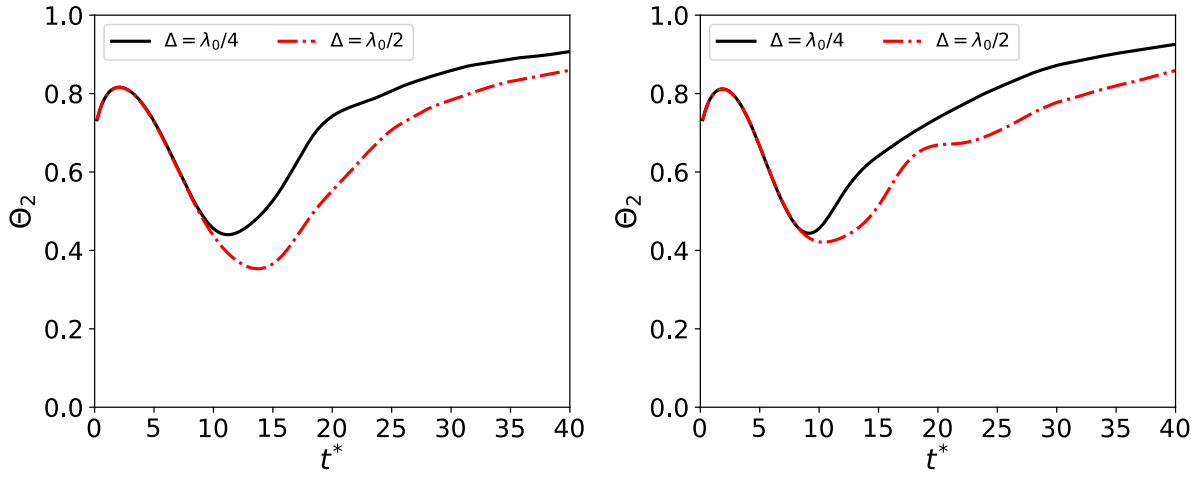

(a) HIL

(b) HLL

(c) HLI

(d) HLH

Fig. 15 Time evolution of the mixedness of fluid 2, Θ_2, for different cases. Black solid line: $\Delta = \lambda_0/4$; red dotted line: $\Delta = \lambda_0/2$.

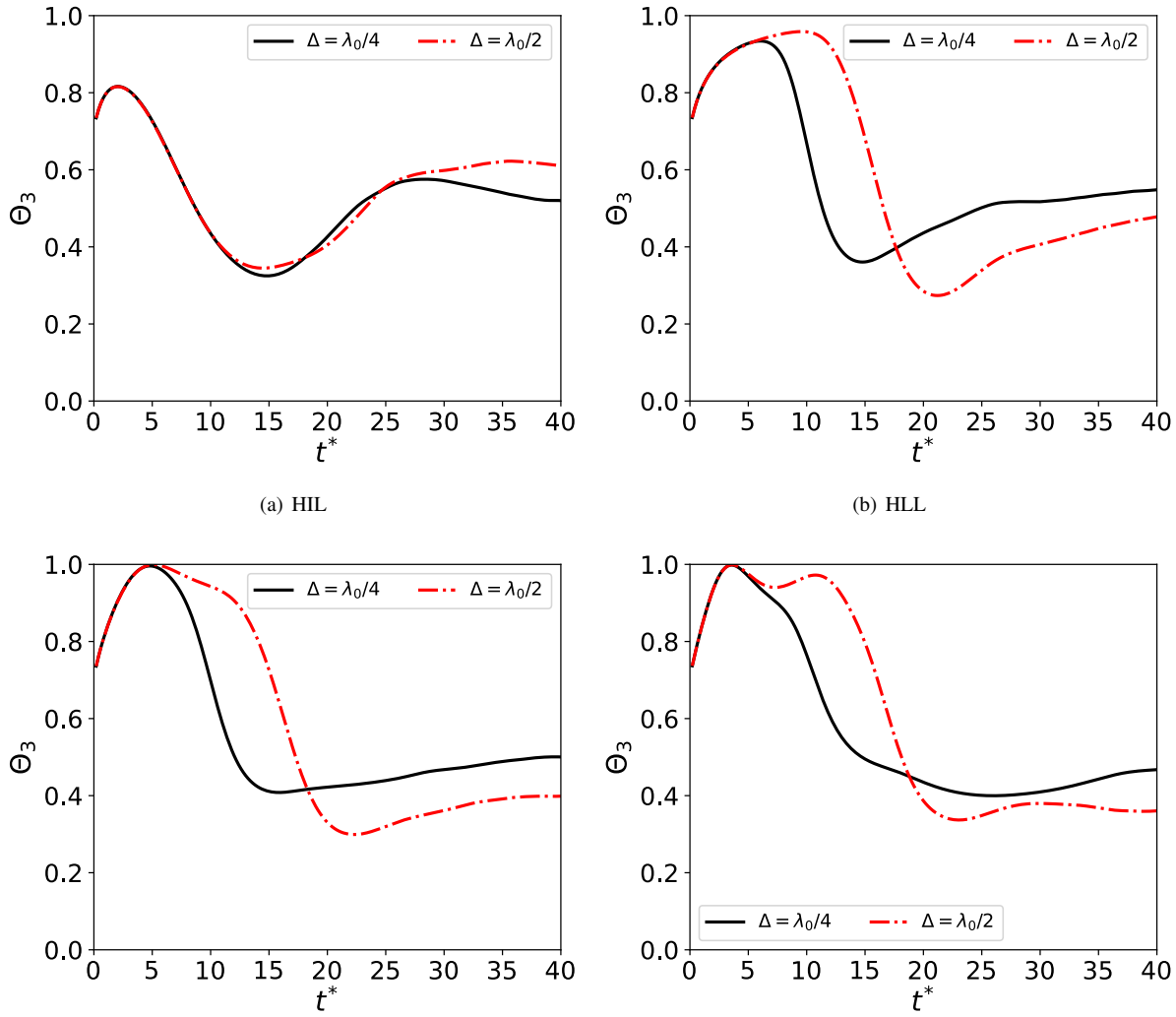

(a) HIL

(b) HLL

(c) HLI

(d) HLH

Fig. 16 Time evolution of the mixedness of fluid 3, Θ_3, for different cases. Black solid line: $\Delta = \lambda_0/4$; red dotted line: $\Delta = \lambda_0/2$.

IV. Conclusion

In this study, three-layer RTI and multi-species mixing were investigated using 2D compressible DNS with an AMR solver. For all cases, the global Atwood number is kept the same, the first (bottom) interface is always RT unstable, and the coupled effects with the second (top) interface stability were explored. It was found that the globally unstable case, HIL, showed a large-scale symmetric mixing during the flow evolution, and its growth behavior quickly becomes like a classic two-layer RTI. While the second (top) interface dynamics are altered by the arrival of the first (bottom) interface, a decrease in the ratio M_2/M_3, which corresponds to a more stable second (top) interface, leads to a slower mixing layer growth behavior and weaker vortical motions in the flow at the later time of the evolution. The DNS cases do not show any sign of the cessation of the mixing layer growth through the mixing widths of fluids 1 and 3, even for the globally stable HLH cases, until the end time of the simulation. This might be attributed to the compressibility effects, although further investigation is required to study the Reynolds number and compressible background stratification effects on three-layer RTI with a longer simulation time in future work.

Acknowledgments

D. A. would like to thank the U.S. National Science Foundation CBET Fluid Dynamics Program (Award No. 2234415) for the financial support that made this work possible. For the computations, this work partially used Stampede2 at the Texas Advanced Computing Center (TACC) through allocation PHY200090 from the Advanced Cyber Infrastructure Coordination Ecosystem: Services & Support (ACCESS) program, which is supported by National Science Foundation grants #2138259, #2138286, #2138307, #2137603, and #2138296.

References

[1] Rayleigh, L., "Investigation of the equilibrium of an incompressible heavy fluid of variable density," *Proceedings of Royal Society of London*, Vol. 14, 1884, pp. 170–177.

[2] Taylor, G., "The instability of liquid surfaces when accelerated in a direction perpendicular to their planes I." *Proceedings of Royal Society of London Series A*, Vol. 201, 1950, pp. 192–196.

[3] Livescu, D., "Turbulence with Large Thermal and Compositional Density Variations," *Annual Review of Fluid Mechanics*, Vol. 52, No. 1, 2020, pp. 309–341.

[4] Aslangil, D., Livescu, D., and Banerjee, A., "Effects of Atwood and Reynolds numbers on the evolution of buoyancy-driven homogeneous variable-density turbulence," *Journal of Fluid Mechanics*, Vol. 895, 2020, p. A12.

[5] Aslangil, D., Livescu, D., and Banerjee, A., "Variable-density buoyancy-driven turbulence with asymmetric initial density distribution," *Physica D: Nonlinear Phenomena*, Vol. 406, 2020, p. 132444.

[6] Sellers, C. L., and Chandra, S., "Compressibility effects in modelling turbulent high speed mixing layers," *Engineering Computations*, Vol. 14, 1997, pp. 5–13.

[7] Schilling, O., "Progress on Understanding Rayleigh-Taylor Flow and Mixing Using Synergy Between Simulation, Modeling, and Experiment," *ASME Journal of Fluids Engineering*, Vol. 142, No. 12, 2020.

[8] Banerjee, A., "Rayleigh-Taylor Instability: A Status Review of Experimental Designs and Measurement Diagnostics," *ASME Journal of Fluids Engineering*, Vol. 142, No. 12, 2020.

[9] Aslangil, D., Banerjee, A., and Lawrie, A., "Numerical investigation of initial condition effects on Rayleigh-Taylor instability with acceleration reversals," *Physical Review E*, Vol. 94, 2016, p. 053114.

[10] Aslangil, D., Farley, Z., Lawrie, A. G. W., and Banerjee, A., "Rayleigh–Taylor Instability With Varying Periods of Zero Acceleration," *Journal of Fluids Engineering*, Vol. 142, No. 12, 2020. 121103.

[11] Aslangil, D., Lawrie, A. G. W., and Banerjee, A., "Effects of variable deceleration periods on Rayleigh–Taylor instability with acceleration reversals," *Phys. Rev. E*, Vol. 105, 2022, p. 065103.

[12] Jacobs, J., and Dalziel, S., "Rayleigh–Taylor instability in complex stratifications," *Journal of Fluid Mechanics*, Vol. 542, 2005, pp. 251–279.

[13] Suchandra, P., and Ranjan, D., "Dynamics of multilayer Rayleigh–Taylor instability at moderately high Atwood numbers," *Journal of Fluid Mechanics*, Vol. 974, 2023, p. A35.

[14] Aslangil, D., and Wong, M. L., "Investigation of strong isothermal stratification effects on multi-mode compressible Rayleigh–Taylor instability," *Physics of Fluids*, Vol. 35, No. 8, 2023.

[15] Wong, M. L., "High-order shock-capturing methods for study of shock-induced turbulent mixing with adaptive mesh refinement simulations," Ph.D. thesis, Stanford University, 2019.

[16] Ramshaw, J. D., "Self-Consistent Effective Binary Diffusion in Multicomponent Gas Mixtures," *Journal of Non-Equilibrium Thermodynamics*, Vol. 15, No. 3, 1990, pp. 295–300.

[17] Williams, F. A., *Combustion theory*, CRC Press, 2018.

[18] Cook, A. W., "Enthalpy diffusion in multicomponent flows," *Physics of Fluids*, Vol. 21, No. 5, 2009.

[19] Berger, M. J., and Colella, P., "Local adaptive mesh refinement for shock hydrodynamics," *Journal of computational Physics*, Vol. 82, No. 1, 1989, pp. 64–84.

[20] Bogey, C., and Bailly, C., "A family of low dispersive and low dissipative explicit schemes for flow and noise computations," *Journal of Computational physics*, Vol. 194, No. 1, 2004, pp. 194–214.

[21] Subramaniam, A., Wong, M. L., and Lele, S. K., "A high-order weighted compact high resolution scheme with boundary closures for compressible turbulent flows with shocks," *Journal of Computational Physics*, Vol. 397, 2019, p. 108822.

[22] Shu, C.-W., and Osher, S., "Efficient implementation of essentially non-oscillatory shock-capturing schemes, II," *Journal of Computational Physics*, Vol. 83, No. 1, 1989, pp. 32–78.

[23] Gunney, B. T., and Anderson, R. W., "Advances in patch-based adaptive mesh refinement scalability," *Journal of Parallel and Distributed Computing*, Vol. 89, 2016, pp. 65–84.

[24] Gunney, B. T., Wissink, A. M., and Hysom, D. A., "Parallel clustering algorithms for structured AMR," *Journal of Parallel and Distributed Computing*, Vol. 66, No. 11, 2006, pp. 1419–1430.

[25] Hornung, R. D., Wissink, A. M., and Kohn, S. R., "Managing complex data and geometry in parallel structured AMR applications," *Engineering with Computers*, Vol. 22, No. 3-4, 2006, pp. 181–195.

[26] Hornung, R. D., and Kohn, S. R., "Managing application complexity in the SAMRAI object-oriented framework," *Concurrency and computation: practice and experience*, Vol. 14, No. 5, 2002, pp. 347–368.

[27] Wissink, A. M., Hornung, R. D., Kohn, S. R., Smith, S. S., and Elliott, N., "Large scale parallel structured AMR calculations using the SAMRAI framework," *Supercomputing, ACM/IEEE 2001 Conference*, IEEE, 2001, pp. 22–22.

[28] Wong, M. L., and Lele, S. K., "Multiresolution Feature Detection in Adaptive Mesh Refinement with High-Order Shock-and Interface-Capturing Scheme," *46th AIAA Fluid Dynamics Conference, AIAA Aviation*, 2016.

[29] Wong, M. L., Livescu, D., and Lele, S. K., "High-resolution Navier-Stokes simulations of Richtmyer-Meshkov instability with reshock," *Physical Review Fluids*, Vol. 4, No. 10, 2019, p. 104609.

[30] Wong, M. L., Baltzer, J. R., Livescu, D., and Lele, S. K., "Analysis of second moments and their budgets for Richtmyer-Meshkov instability and variable-density turbulence induced by reshock," *Physical Review Fluids*, Vol. 7, No. 4, 2022, p. 044602.

[31] Wong, M. L., and Lele, S. K., "High-order localized dissipation weighted compact nonlinear scheme for shock-and interface-capturing in compressible flows," *Journal of Computational Physics*, Vol. 339, 2017, pp. 179–209.

[32] Prine, T., Aslangil, D., and Wong, M. L., "Coupled Effects of Iso-thermal Stratification Strength and Atwood Number on 2D Single-Mode Compressible Rayleigh–Taylor Instability," *AIAA SCITECH 2023 Forum*, 2023, p. 1044.